MODELLING AND CONTROL OF A MeerKAT ANTENNA

I. Dodia[†], South African Radio Astronomy Observatory, Cape Town, South Africa
also at University of Cape Town, Cape Town, South Africa

Abstract

This paper presents a comprehensive approach to modelling for control system design for a MeerKAT antenna. It focuses on dynamic modelling using time and frequency domain techniques, and lays the foundation for the design of a control system to meet the telescope's stringent pointing and tracking requirements. The paper scope includes rigid body modelling of the antenna, system identification to obtain model parameters, and building a system model in Simulink. The Simulink model allows us to compare model performance with the measured antenna pointing, under various environmental conditions. The paper also integrates models for pointing disturbances, such as wind and friction. The integrated model is compared to the existing control setup. Wind disturbance plays a significant role in the pointing performance of the antenna, therefore the focus is placed on developing an appropriate wind model.

This research will conclude by providing a well-documented, systematic control system design that is owned by SARAO and can be implemented to improve the pointing performance of the telescope.

INTRODUCTION

The MeerKAT Radio Telescope located in South Africa's Northern Cape province is a precursor instrument to the Square Kilometre Array (SKA) project. MeerKAT consists of 64 antennas each with 13.5 m dish structures. The antennas are arranged in a spiral array with a maximum baseline (point-to-point distance between antennas) of 8 km. MeerKAT observes in a range of frequencies ranging from about 500 MHz to upwards of 4 GHz with the use of multiple receiver systems. The telescope was commissioned in 2018 and is in active use.

Each antenna can move to point its dish in two axes: azimuth and elevation. Due to the large dish size and tight requirement specifications, pointing an individual antenna is a critical component in achieving optimal imaging fidelity. Antenna pointing and tracking is done by the Antenna Positioner (AP) subsystem - a commissioned "black box" subsystem that was integrated into MeerKAT during the telescope's development.

Now that MeerKAT is in its operational phase, issues related to the AP subsystem are being uncovered; without a comprehensive understanding of the design, troubleshooting and resolving these issues is challenging. This paper focusses on building a comprehensive model of the mechanical dynamics of the AP system, considering parameter uncertainty and accurately capturing disturbances. This will lay the foundation for future work towards a systematic feedback design for MeerKAT.

---

† idodia@sarao.ac.za

BACKGROUND

Drive Configuration

The individual antennas of the MeerKAT telescope use a 13.5 m Gregorian offset dish, configured in an elevation over azimuth arrangement. A pedestal provides a foundation on which a yoke is attached to achieve this configuration. Figure 1 identifies the major drive components of a MeerKAT antenna.

Rotation in the azimuth axis of the antenna is achieved by the use of two motor drives that are attached to the yoke structure. Each motor drive consists of a servo drive with a high stiffness, low friction planetary gearbox that drives output pinions. These pinions interface with the outer teeth of the static azimuth gear and drive the entire yoke (and elevation structure) in azimuth. The motor drives are electronically torque biased to minimise backlash. Figure 2 highlights the key components of the azimuth drive assembly. This drive configuration is typical in high precision radio astronomy applications [1]. An azimuth on-axis encoder is located inside the pedestal and reads out the position of the antenna in azimuth for the control loop.

Rotation in the elevation axis is achieved by means of a jackscrew drive (ball screw driven by a torque servo motor) that is mounted on the yoke and attaches to the back of the main reflector on the back up structure. Mechanical preloading of the jackscrew drive is done to minimise backlash. Linear actuation of the jackscrew causes rotational movement of the main reflector around a pivot point. Counterweights attached to the back up structure maintain the centre of mass of the dish to be about this pivot point, ensuring that there is no resulting unbalanced load torque on the elevation axis. The elevation encoder is also located on the axis of this pivot point, as shown in Fig. 2.
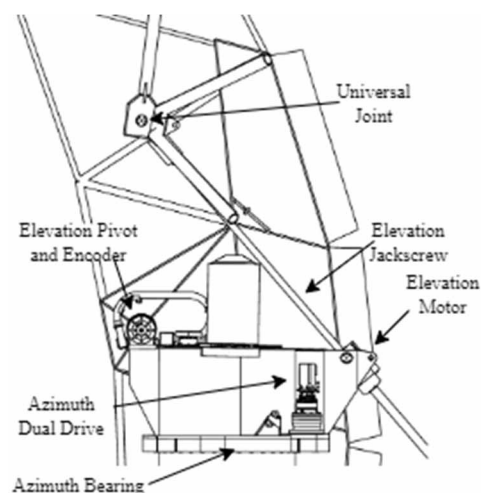

Figure 1: Azimuth and elevation drive assemblies, drawing taken from [1].

19th Int. Conf. Accel. Large Exp. Phys. Control Syst.   ICALEPCS2023, Cape Town, South Africa   JACoW Publishing

ISBN: 978-3-95450-238-7   ISSN: 2226-0358   doi:10.18429/JACoW-ICALEPCS2023-M03A004
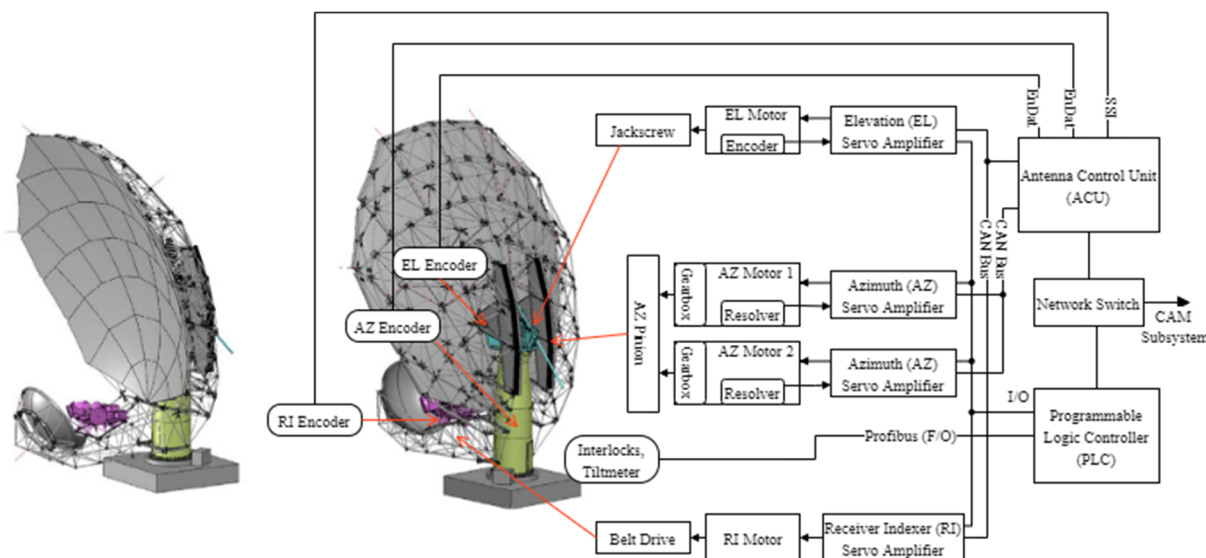
Figure 2: MeerKAT antenna structure and drive configuration overview, with dish renders taken from [1].

Current Control Architecture

The control and monitoring of the MeerKAT telescope can be broken into two primary components: the Control and Monitoring (CAM) and AP systems. The CAM subsystem provides an interface for the remote monitoring and control of the telescope. High level commands are provided through the CAM subsystem to the AP subsystem, and various monitoring sensors on the antennas feed data back. The AP subsystem provides low level control of the antenna pointing and its primary component is the Antenna Control Unit (ACU); a dedicated PC-based system that interacts with various sensors and drives to actuate the antenna.

Alongside providing an interface to command and monitor the telescope, the CAM subsystem employs a Pointing Model to correct for systematic errors such as thermal deformation to the antenna structure and tilt of the antenna pedestal. The Pointing Model provides the command position to the AP subsystem. The AP subsystem takes the command position, computes the error based on the current encoder read out in elevation and azimuth and actuates the servo drives to correct for this error.

Figure 3 shows a high-level block diagram of the implemented control architecture for the azimuth and elevation axes. The implemented digital controller includes features of high bandwidth loops for wind disturbance rejection, acceleration feedforward for maximum dynamic bandwidth, anti-overshoot and fast step-settling features, anti-limit cycle architecture, and backlash compensation.

A cascaded control architecture is employed. The innermost current loop has a closed loop bandwidth of 100 Hz; subsequent velocity and position loops have bandwidths of about 10-15 Hz and 0.5-1 Hz respectively.

A Command Profiler is used to damp large position overshoots as a result of the high gain loops. It is only active when position steps are applied, not when tracking. The outermost position loop takes the encoder readout and computes the position error, and accounts for velocity and acceleration saturation limits. The output of the position controller is summed with the velocity feedforward signal and is fed into the velocity loop.
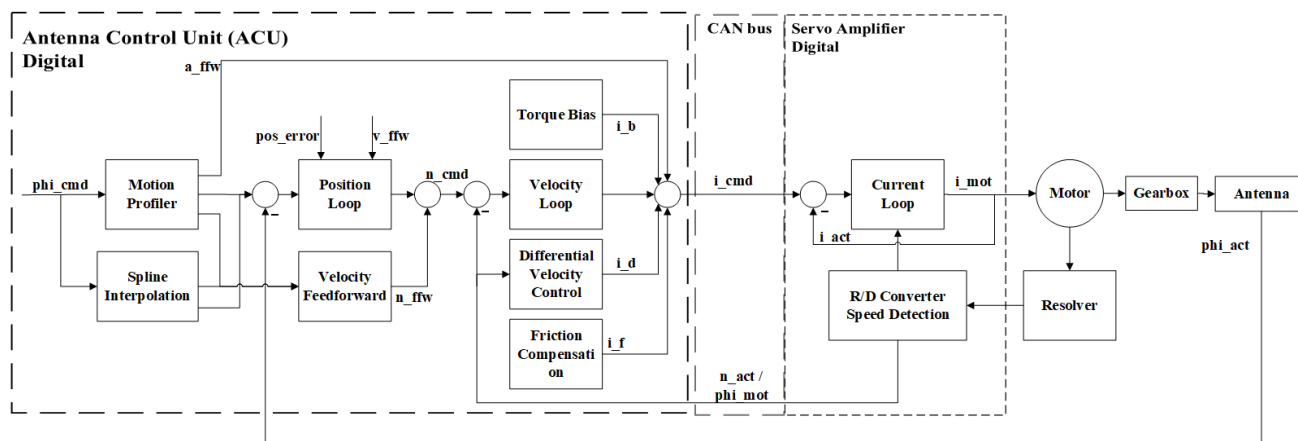

Figure 3: Current control architecture for the AP subsystem on MeerKAT.

The velocity loop uses a PI controller. In the case of the azimuth axis, a superimposed differential speed controller and a torque bias are used to compensate for friction and backlash in the azimuth drive. In the elevation axis, a constant direction dependent torque feedforward is applied in order to overcome the inherent friction of the jackscrew.

Pointing and Tracking Requirements

During a typical observation, a set of antennas will be pointed at the source of interest for a while and will periodically be stepped away to acquire a reference source for calibration. Sources are tracked at the sidereal rate (approximately 4 mdeg/s), the rate of movement of celestial objects across the sky as the Earth spins. The following are the relevant MeerKAT design specifications [2].

- Req. 1) Pointing jitter whilst tracking: The AP, under Optimal Operating Conditions and after centering the Beam Axis on a reference source, shall track the reference source over a period of at least 10 seconds, with a pointing jitter of less than 15 arcsec RMS.
- Req. 2) Change Source at maximum slew speed: The AP moving at maximum slew speed under Optimal Operating Conditions shall settle on a Command Source Direction within pointing jitter requirements specified in Req. 1, in less than 15 seconds.
- Req. 3) Step Responses of 4 degrees (Change Source): The AP under Optimal Operating Conditions, after centering the Beam Axis on a reference target and then moving 4 degrees away, shall return to the reference target and settle to the pointing jitter requirements specified in Req. 1, in less than 10 seconds.
- Req. 4) Step Responses of 30' (Change Source): The AP under Optimal Operating Conditions, after centering the Beam Axis on a reference target and then moving 30' away, shall return to the reference target and settle to the pointing jitter requirements specified in Req. 1, in less than 4 seconds.
- Req. 5) Sidereal Tracking at 4 mdeg/s under normal operating conditions: The AP shall meet tracking requirements for targets moving at rates of 0 to 0.04 degrees per second in both axes from 15 to 88 degrees in elevation.

Optimal operating conditions are defined as sustained minute mean wind speed ≤ 2.9 m/s and 3-second wind gust ≤ 4.1 m/s. Normal operating conditions are defined as sustained 5-minute mean wind speed ≤ 9.8 m/s and 3-second wind gust ≤ 13.4 m/s.

Attention is drawn to the difference between the Beam Axis (defined as "the axis through the vertex of the parabola of the Main Reflector parallel to the Reflector Beam Direction") and the Reflector Beam (defined as "the spherical coordinates of the peak of the Reflector Beam referenced to the Reflector Coordinates", i.e. the RF Beam).

SYSTEM MODELLING

System modelling of the mechanical dynamics of the antenna involves developing independent models for the azimuth and elevation axes, which are then later integrated.

Once an analytical expression is developed, with the help of a Simulink model, frequency domain system ID techniques are employed to verify the supplier quoted design parameters against actual measurements.

Analytical Model

The modelling approach uses a two-mass model with compliance to capture the (anti-)resonant behaviour between the driving motors and the antenna structure. This model form is relevant to both the azimuth and elevation axes.

A block diagram of a two-mass system with compliance and friction is shown in Fig. 4. The command current (I_C) from the output of the current controller is multiplied by the motor torque constant (K_ϕ) to generate a driving torque (T_E). The motor torque (T_M) is used to accelerate the motor, which has inertia (J_M). The motor acceleration (A_M) is integrated to give the motor speed (V_M) and then further integrated to give motor position (P_M). V_M is fed back through the motor friction (B_M). The difference between the V_M and the load speed (V_L), and P_M and the load position (P_L) are multiplied by the cross coupled viscous damping (K_{CV}) and shaft stiffness (K_s) respectively and then summed to generate the load torque (T_L). This torque acts on the load inertia (J_L) to accelerate the load (A_L).
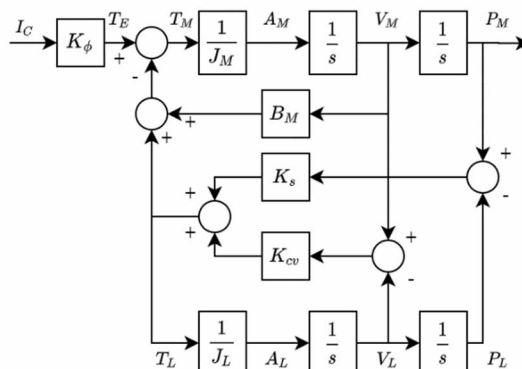

Figure 4: Two-mass model block diagram with resonant load.

With respect to the azimuth axis, two motors are used to drive the structure (load). By assuming both motors to be identical, the model shown in Fig. 4 is modified by simply doubling each motor parameter.

Additionally, the block diagram shows all the motor and load parameters as seen from one side of the gearbox: the load inertia and friction are *reflected* through any scaling factors N (motor gearbox and pinion-azimuth bearing) by dividing by N^2. As a result of the large gear ratio between the motor and the structure, the reflected inertia and friction of the large antenna structure is seen as comparable in magnitude to that of the motor.

Based on Fig. 4, the following matrix expression can be written to describe the T_E in terms of P_M and P_L:

$$\begin{bmatrix} T_E \\ 0 \end{bmatrix} = \begin{bmatrix} J_M s^2 + (B_M + K_{cv})s + K_s & -(K_{cv}s + K_s) \\ -(K_{cv}s + K_s) & J_L s^2 + K_{cv}s + K_s \end{bmatrix} \begin{bmatrix} P_M \\ P_L \end{bmatrix}$$

Writing this expression out in terms of the P_M gives

$$\frac{P_M}{T_E} = \frac{1}{(J_M+J_L)s^2+B_M s}\left\{\frac{A}{B}\right\} \tag{1}$$

where

$$A = J_L s^2 + K_{cv} s + K_s$$

and

$$B = \left(\frac{J_M J_L}{(J_M+J_L)s+B_M}\right)s^2 + \left(\frac{J_M K_{cv}+J_L(B_M+K_{cv})}{(J_M+J_L)s+B_M}\right)s + \frac{B_M K_{cv}+(J_L+J_M)K_s}{(J_M+J_L)s+B_M} + \frac{B_M K_s}{(J_M+J_L)s^2+B_M s}$$

The terms outside the braces in Eq. 1 gives us the rigid body model of the system (i.e. without the shaft compliance). The anti-resonance frequency (when the compliant expression shows a trough, see Fig. 5) is when the numerator from Eq. 1 is at its minimum value. This shows that the anti-resonance frequency F_{AR} is dependent on the drive stiffness and load inertia. The peak of the (anti-)resonance is related to the K_{cv} term.
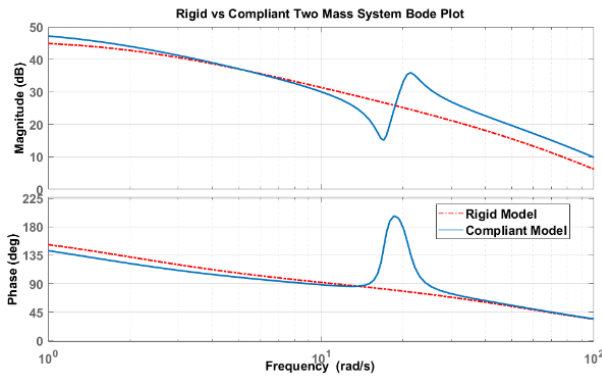
$$F_{AR} = \sqrt{\frac{K_s}{J_L}}\, rad/sec$$

Figure 5: Rigid vs Compliant two mass system bode plot, using Azimuth design values at 15 degrees elevation.

The effect of the anti-resonance is that control action is limited at that frequency. Parameter uncertainty is introduced in the elevation axis due to the drive configuration: the jackscrew length values over the elevation range, thus changing the stiffness of the coupling between the driving motor and the structure. The load inertia of the azimuth axis also varies over the elevation range, however is constant for the elevation axis as the dish rotates about its centre of mass.

This creates a range of possible behaviour of the dynamics depending on where the antenna is pointing. Thus using Figs. 3 and 4, and the design documentation as reference for motor and load parameters, Simulink models for the azimuth and elevation were created. The benefit of this is that the control features present in the system (torque bias, for example) as well as disturbances can be integrated and tested. This can be used to compare against the actual dynamics of the antenna and help build a wholistic model that incorporates parameter variation.

System ID

Once the analytical forms of the azimuth and elevation axes are understood, the next step is to investigate how well the actual system matches the design parameters, in both open loop and closed loop.

To do this, initially a time domain approach was used by means of studying step responses in the azimuth and elevation axes. Testing was executed remotely through the CAM system. Doing it this way meant that the system could only be run in closed loop. The AP data logs, particularly the motor currents and encoder positions were captured during testing. These logs were accessed via the CAM system interface, which logs certain PLC and ACU data amongst other data points. This data was then cleaned and subsequently processed using Matlab's system ID toolbox, using the motor current as the input and encoder positions as the outputs. The open loop models were then derived by inverting the closed loop model and using the documented PID values. This method proved ineffective in deriving the actual system parameters as there was significant mismatch between derived values and designed values.

The limitations of this approach were that performing the step responses via the CAM system meant that the system had to be run in closed loop, with control features such as the differential velocity control, feedforward and motion profiler still active. This method proved challenging due to not not having full access within the ACU to safely remotely turn of controller features.

Hence the next technique was to locally drive an antenna in open loop with the ACU velocity controller turned off. Frequency domain techniques were then employed to derive the input-output relationship of the velocity loop. This was done by means of injecting a Gaussian white noise signal that was superimposed to a constant velocity command, which would overcome the static friction of the system and ensure that the system was in a linear regime. Frequency domain approaches also lend themselves well to investigating the resonant behaviour of the system. The ACU provides test output points which provide a scaled analogue output of the motor speeds directly from the servo amplifiers.

By comparing the Simulink model response against the experimental data, good model matching was found with slight variations in frequency features over the range of elevation, in both axes. Furthermore, by closing the velocity loop in the Simulink model using the documented PI control values, the closed loop response of the system can be simulated. Shown below are the magnitude and phase responses for the azimuth axis at 15 degrees elevation, in both open and closed loop (Fig. 6 and Fig. 7, respectively), and for the elevation axis at 15 degrees elevation (Fig. 8 and Fig. 9, respectively). The experimental values for inertia and friction in both axes match the quoted values, as is evident by studying the low frequency behaviour of the plots below, where the rigid body model is more dominant. However, there is a mismatch of the anti-resonant frequency, indicating a variation of K_s of up to 30% in

azimuth and 20% in elevation across the antenna travel range. This likely due to the quoted K_s terms accounting only for the motor drive shaft and not for the entire drive configuration stiffness.
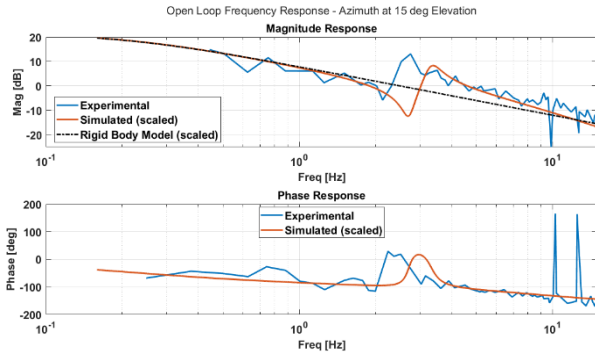

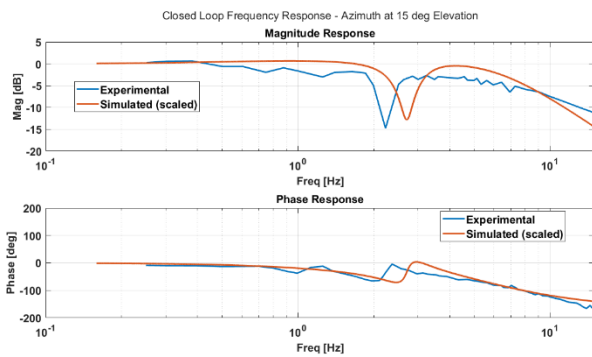Figure 6: Open Loop - Azimuth at 15 degrees elevation.

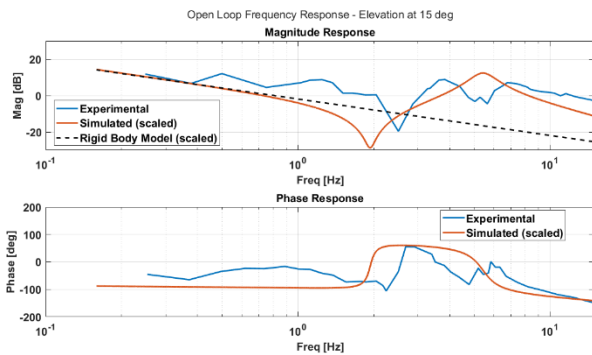Figure 7: Closed Loop - Azimuth at 15 degrees elevation.
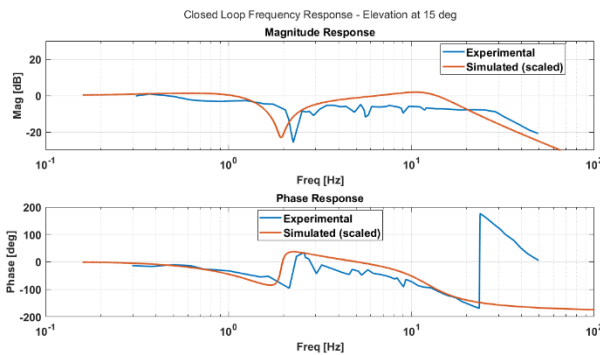

Figure 8: Open Loop - Elevation at 15 degrees.

Figure 9: Closed Loop - Elevation at 15 degrees.

DISTURBANCE MODELLING

Wind loading of the antenna dish structure is a major cause of pointing and tracking disturbances in large radio telescopes [3, 4]. Despite wind spectra being dominated by low frequency components, higher frequency antenna modes can be excited which can result in significant error [5]. Hence, it is critical to develop an understanding of wind dynamics and the effect of the induced disturbances.

Wind Models

Wind velocity $v = v_m + v_t$ is modelled by two components: a steady state mean velocity, v_m; and a gust velocity, v_t, which is a zero mean stochastic process with standard deviation σ_v.

To describe wind velocity various Power Spectral Density (PSD) expressions that describe the spectral content of the wind being modelled have been defined in the literature. Focus is made on modelling the wind running parallel to the ground. The Davenport wind spectrum model will be considered as it is typically used in radio telescope disturbance modelling, see [4, 6].

The Davenport spectrum is defined for a mean wind speed v_m as

$$S_d(\omega) = 4800 v_m \kappa \left(\frac{\beta\omega}{(1+\beta^2\omega^2)^{\frac{4}{3}}} \right) \quad (2)$$

where $\beta = \frac{600}{\pi v_m}$ and the terrain surface drag coefficient κ is given by

$$\kappa = \frac{1}{\left(2.5 \, ln\left(\frac{z}{z_0}\right) \right)^2}$$

In the expression above, z is the height at which the spectrum is to be defined, and z_0 is the terrain height.

To implement this spectrum as a linear system, white noise with unit standard deviation is passed through a shaping filter to produce coloured noise with the related spectral content. An approximate filter realisation is needed as spectral factorisation leads to no exact linear transfer function for the Davenport spectrum.

Using Eq. 2 and setting $z = 10 \, m$ as the height of the anemometer on site for comparison to measured data, $z_0 = 0.4 \, m$ as the on-site terrain height estimate (sparse shrubs), and for the two cases of $v_m = 3 \, m/s$ and $v_m = 9.5 \, m/s$ the following filter approximation transfer functions were derived:

$$H_3(s) = \frac{2.93s^3 + 203.5s^2 + 978s + 3.616}{0.662s^4 + 76.6s^3 + 1056s^2 + 38.7s + 0.248}$$

$$H_{10}(s) = \frac{3.95s^3 + 370.8s^2 + 947.1s + 5.12}{0.333s^4 + 38.4s^3 + 229s^2 + 23.6s + 0.346}$$

Employing a Simulink model, white noise was passed through the shaping filters defined above to output the simulated windspeeds shown in Fig. 10. The performance of the Davenport model to generate a time-varying wind speed signal dependent on the mean wind speed that matches the wind profile on the MeerKAT site is thus satisfactory.
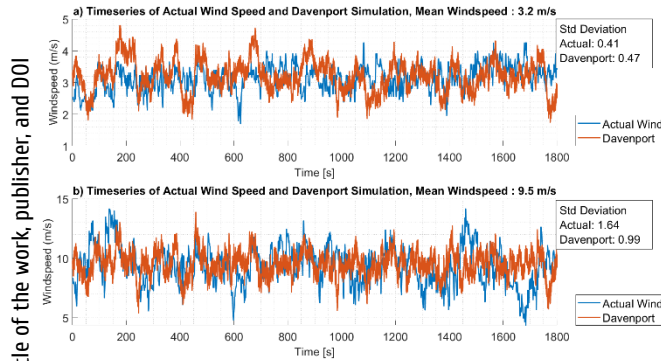
Figure 10: Time domain comparison of actual wind speed against simulated wind speed.

Antenna Loading

Wind hitting the surface of the antenna dish structure causes various forces and moments to be generated, which are shown in Fig. 11. Only the pitching and yawing moments are considered here as the other moments are reacted to by the dish backup structure and not directly by the drives. Furthermore, wind loading on the antenna causes deformation to the dish structure which affects the pointing accuracy of the beam; however, this falls outside the scope of this research as these errors are not seen by the axis drives.
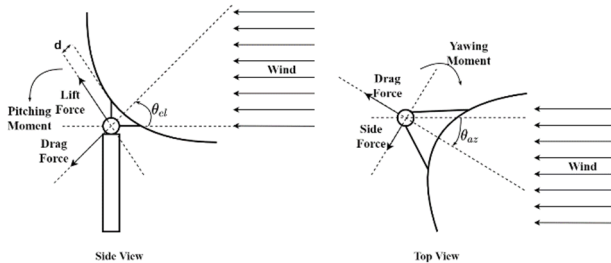
Figure 11: Wind force and torque loading on antenna structure.

The pitching and yawing moments are proportional to the off-centre force applied that causes a torque around the corresponding axis. This can be expressed as a dimensionless torque coefficient τ, defined in [7] as

$$\tau = \frac{T}{0.5\rho v_m^2 AD} \qquad (3)$$

Where v_m is the mean windspeed, T is the applied on-axis torque; $A = \pi \frac{D^2}{4}$, the frontal surface area of the dish (seen as a circle); D is the diameter of the dish; and, ρ is the static air density.

Thus, torque coefficients can be defined for both the pitching (elevation) τ_{el} and yawing (azimuth) τ_{az} axes. The values of the coefficients are unique for each antenna, and are dependent on the elevation and azimuth angle of the antenna with respect to the wind direction. Through experimentation, the range of values for τ_{el} and τ_{az} were determined for a MeerKAT antenna.

To do this, a day when there was a steady mean wind speed of about 5 m/s was selected for testing. For the yawing coefficients, an antenna fixed at a range of elevation angles (15° to 90° in 15° increments) and then rotated 360°

in azimuth at a rate of 0.2 deg/s. Similarly, for the pitching coefficients an antenna was fixed at a range of azimuth angles (-90° to 225° in 45° increments) and then elevated from 15° to 90° at a rate of 0.2 deg/s. The rate chosen for this experiment was balanced between the need to complete the testing fast enough to ensure that the wind conditions remained constant throughout the test, as well as to operate in a linear friction regime. Using Eq. 3 to compute τ_{el} and τ_{az} for the range of elevation and azimuth angles, the yawing and pitching coefficients can be found. As shown in Fig. 12 and Fig. 13 a surface can be fit to the data that can be used to estimate the yawing and pitching coefficients for any given elevation and azimuth angle.
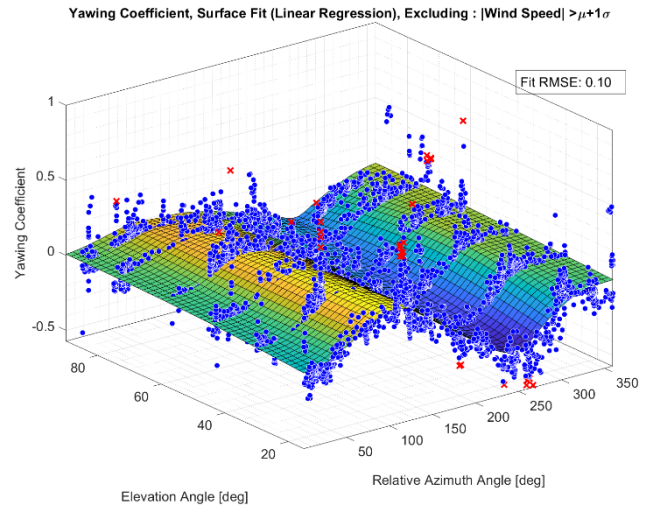

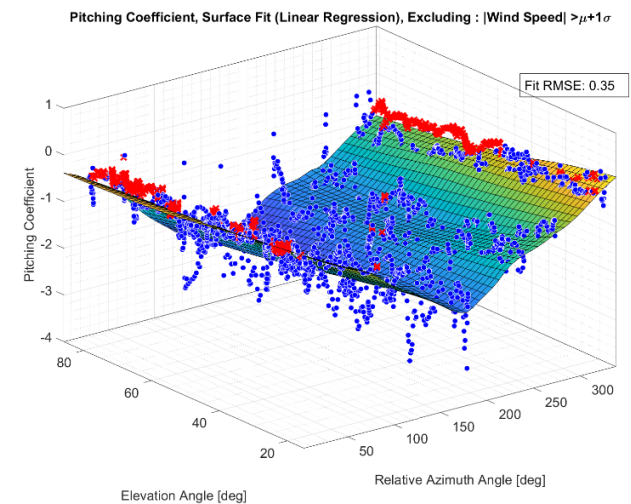Figure 12: Yawing coefficient surface fit.

Figure 13: Pitching coefficient surface fit.

However, Eq. 3 is defined for steady state wind. Figure 14 shows how the approach used to generate wind torque disturbances T_w for a given gusting wind disturbances Δv_0, using a scale factor k_t, as described in [8]

$$T_w = k_t \Delta v_0.$$

The scaler k_t is defined with reference to the motor axis referred through a gearbox ratio N as and τ as either τ_{el} or τ_{az} depending on the axes being calculated for

$$k_t = \frac{2(\tau 0.5 \rho AD)\sqrt{6\kappa}}{N} v_m^2.$$
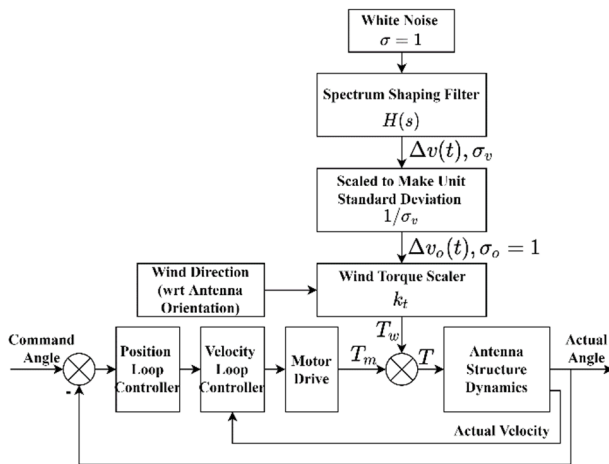

Figure 14: Wind disturbance modelling acting on motor torques, block diagram.

Based on Fig. 14, the Simulink model incorporated the wind disturbances, with one of the use cases simulated shown in Fig. 15.
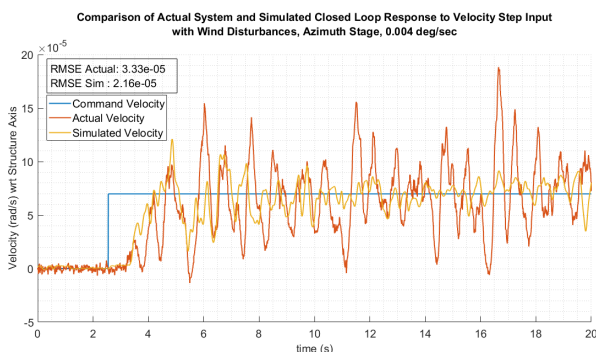

Figure 15: Actual vs Simulated wind disturbance tracking at 0.004 deg/s in Azimuth.

By inspection the results look plausible. The higher error seen on the actual system could be related to the antenna running close to the static friction limit, which is challenging to accurately capture in the model. Additionally, the unmodelled effects of the lift and drag forces highlighted in Fig. 11 may be a cause of further mismatch. Nonetheless, the approach followed to use the Davenport spectrum to simulate windspeed and then incorporate the gusting torque disturbances into the Simulink antenna model produces satisfactory results. Furthermore, an appreciation of the disturbance spectrum has been furthered, which will prove to be critical in the controller design phase.

CONCLUSIONS AND FUTURE WORK

This paper presents the work done in developing a comprehensive model of the dynamics of a MeerKAT antenna,

in the elevation and azimuth axes. Effort has been made to develop a thorough understanding of model uncertainty and disturbances. In particular focus was made on simulating the on-site wind profile and the resultant antenna loading, which is primarily responsible for affecting pointing performance. System ID techniques were used to verify design parameters and uncover mismatch between the quoted and actual values of the system. A Simulink model was created to incorporate these design and disturbance features. The resultant model showed good correlation with the real system, in both the time and frequency domains.

This work is part of a larger effort to engage in a systematic design process of a feedback controller for the MeerKAT telescope, that accounts for uncertainty, minimises disturbances and ultimately achieves the tight pointing and tracking requirements.

ACKNOWLEDGEMENTS

REFERENCES

[1] R. Masey, "13.5m MeerKAT dual offset antenna system description document," Vertex Antennentechnik GmbH, Description Document OD-1012033-01-01, Oct. 15, 2014.

[2] H. Bester, "MeerKAT antenna positioner requirement specification," South African Radio Astronomy Observatory, Requirement Specification, Oct. 29, 2013.

[3] M. F. Campbell, "Critical wind effects on parabolic reflectors," in *Proc. SPIE 5495*, Astronomical Structures and Mechanisms Technology, J. Antebi and D. Lemke, Eds., USA, Sep. 29, 2004, p. 549. doi:10.1117/12.552352

[4] W. Gawronski, B. Bienkiewicz, and R.E. Hill, "Wind-induced dynamics of a deep space network antenna," *J. Sound Vib.*, vol. 178, no. 1, pp. 67-77, Nov. 1994. doi:10.1006/jsvi.1994.1468

[5] W. Gawronski, *Modeling and Control of Antennas and Telescopes*, ser. Mechanical Engineering Series. Boston, MA: USA: Springer, 2008.

[6] Z.-F. Shao, X. Tang, L.-P. Wang, and X. Chen, "Dynamic modeling and wind vibration control of the feed support system in FAST," *Nonlinear Dyn.*, vol. 67, no. 2, pp. 965–985, Jan. 2012. doi:10.1007/s11071-011-0040-4 E

[7] E. Simiu and R. Scanlan, *Wind Effects on Structures*, 3rd ed. New York: John Wiley & Sons, Inc., 1996.

[8] W. Gawronski, "Three models of wind-gust disturbances for the analysis of antenna pointing accuracy," IPN Progress Report, pp. 42-149, May 2002.